

An X-ray investigation of the NGC 346 field in the SMC (2) : the field population

Y. Nazé^{1,2}, J.M. Hartwell³, I.R. Stevens³, J. Manfroid^{1,4,5}, S. Marchenko⁶, M. F. Corcoran⁷,
A.F.J. Moffat⁸, G. Skalkowski⁸

ABSTRACT

We present results from a *Chandra* observation of the NGC 346 cluster, which is the ionizing source of N66, the most luminous H II region and the largest star formation region in the SMC. In the first part of this investigation, we have analysed the X-ray properties of the cluster itself and the remarkable star HD 5980. But the field contains additional objects of interest. In total, 75 X-ray point sources were detected in the *Chandra* observation: this is five times the number of sources detected by previous X-ray surveys. We investigate here their characteristics in detail. Due to high foreground absorption, the sources possess rather high hardness ratios. Their cumulative luminosity function appears generally steeper than that for the rest of the SMC at higher luminosities. Their absorption columns suggest that most of the sources belong to NGC 346. Using DSS data and new *UBVRI* imaging with the ESO 2.2m telescope, we also discovered possible counterparts for 32 of these X-ray sources and estimated a B spectral type for a large number of these counterparts. This tends to suggest that most of the X-ray sources in the field are in fact X-ray binaries. Finally, some objects show X-ray and/or optical variability, with a need for further monitoring.

Subject headings: (galaxies:) Magellanic Clouds–X-rays: individual (NGC 346)

¹Institut d'Astrophysique et de Géophysique, Université de Liège, Allée du 6 Août 17, Bat. B5c, B 4000 - Liège (Belgium); naze@astro.ulg.ac.be, manfroid@astro.ulg.ac.be

²Research Fellow F.N.R.S.

³School of Physics & Astronomy, University of Birmingham, Edgbaston, Birmingham B15 2TT (UK); jmh@star.sr.bham.ac.uk, irs@star.sr.bham.ac.uk

⁴Research Director F.N.R.S.

⁵Visiting Astronomer, European Southern Observatory

⁶Department of Physics and Astronomy, Thompson Complex Central Wing, Western Kentucky University, Bowling Green, KY 42101-3576 (USA), sergey@astro.wku.edu

⁷Universities Space Research Association, High Energy Astrophysics Science Archive Research Center, Goddard Space Flight Center, Greenbelt, MD 20771; corcoran@barnegat.gsfc.nasa.gov

⁸Département de physique, Université de Montréal, C.P. 6128, Succ. Centre-Ville, Montréal, QC, H3C 3J7 (Canada); moffat@astro.umontreal.ca, gwen@astro.umontreal.ca

1. Introduction

The launch of the *Chandra* satellite provides an opportunity to explore the X-ray sky with a far greater sensitivity and spatial resolution than ever before. In a given field of interest, these characteristics enable the discovery of numerous X-ray sources in addition to the main target(s). Although often regarded as secondary, these sources provide important information which can improve our knowledge of the X-ray emission mechanisms in the Universe.

These serendipitous discoveries also enable us to study the source distribution in galaxies, especially Magellanic dwarf galaxies in our case. Most of the dwarf galaxies studied are at a distance of a few Mpc (e.g. Martin, Kobulnicky, & Heckman 2002), and their X-ray observations only sample the population with $L_X > 10^{36}$ erg s⁻¹. On the other hand, the relative closeness of the

Magellanic Clouds enable us to probe the X-ray sources with luminosities as low as 10^{32} erg s $^{-1}$. Putting together the informations on faint and bright X-ray sources will ultimately lead to a better understanding of this type of galaxies.

We have obtained a deep *Chandra* observation of the giant H II region N66 (Henize 1956), the largest star formation region in the Small Magellanic Cloud (SMC). The large number of massive stars and the presence of the remarkable star HD 5980 make the NGC 346 field one of the best opportunities to conduct an investigation of the X-ray domain.

In the first part of this analysis (Nazé et al. 2002, paper I), we have presented the characteristics of the cluster, the star HD 5980 and its close neighborhood. The cluster itself is relatively faint and most of its emission seems correlated with the location of the brightest stars in the core. However, the level of X-ray emission could not be explained solely by the emission from individual stars. The *Chandra* observation also provides the first X-ray detection of HD 5980. In X-rays, the star, that underwent a LBV-type eruption in 1994, appears very bright, comparable only to the brightest WR stars in the Galaxy. This high luminosity could be explained either by colliding winds in the binary system or by post-eruption effects. Finally, a bright, extended X-ray emission seems to surround this star. It is probably due to a SNR which may or may not be related to HD 5980 itself (see paper I).

In this second paper, we will focus on the other X-ray sources present in the field. First, we will describe in § 2 the observations used in this study. The detected sources, their hardness ratios (HRs), and their spectral characteristics will then be discussed in § 3, 4, and 5, respectively. Next, we will describe the overall properties of the point sources' population in § 6, present their possible counterparts in § 7 and investigate their variability in § 8. Finally, we will give a summary in § 9.

2. The Observations and Data Analysis

2.1. X-ray Observations

NGC 346 was observed with *Chandra* for the XMEGA⁹ consortium on 2001 May 15–16 for 100 ks (98.671 ks effective, ObsID = 1881, JD~2452045.2). The data were recorded by the ACIS-I0, I1, I2, I3, S2 and S3 CCD chips maintained at a temperature of -120°C . The data were taken with a frame time of 3.241s in the faint mode. Our faintest sources have fluxes of about 6×10^{32} erg s $^{-1}$ (see §6), assuming a distance of 59 kpc for the SMC (Mathewson et al. 1986). More details about the processing of the data can be found in paper I.

For long exposures, removing the afterglow events can adversely affect the science analysis (underestimation of the fluxes, alteration of the spectra and so on, see paper I). We thus computed a new level 2 events file and we will use this new file throughout this paper, except for the source detection, where it is better to use the pipeline level 2 product to avoid mistaking afterglow events for real sources.

Further analysis was performed using the CIAO v2.1.2 software provided by the CXC and also with the FTOOLS tasks. The spectra were analysed and fitted within XSPEC v11.0.1 (Arnaud 1996). Fig. 1 shows an image of the four ACIS-I chips : numerous point sources and some diffuse emission near HD 5980 can be seen. Fig. 2 presents the superposition of the *Chandra* data on a DSS image. The ACIS-I field-of-view covers $290 \text{ pc} \times 290 \text{ pc}$, while the size of NGC 346 is $180 \text{ pc} \times 220 \text{ pc}$ (Ye, Turtle, & Kennicutt 1991). Note that due to their high noise and poor resolution, the ACIS-S data won't be analysed in details here.

2.2. WFI Images

Optical imaging data were acquired as part of a project aiming at the photometric calibration of the Optical Monitor on board the ESA satellite *XMM-Newton* (Mason et al. 2001). The NGC 346 field was among the selected fields ob-

⁹<http://lheawww.gsfc.nasa.gov/users/corcoran/xmega/xmega.html>

served by *XMM-Newton* that were photometrically calibrated on the basis of ground-based observations.

The images of this field were obtained in April 2001 at the MPG/ESO 2.2-m telescope with the WFI mosaic camera¹⁰ providing a field of view of 0.5×0.5 square degrees. Due to the unfavorable position of the SMC at this period of the year, the seeing was less than perfect but the data quality was still good. The total exposure times were 25 minutes in the *U*-band and about 10 minutes in the other bands (*BVRI*). The reductions were performed with IRAF and our personal software. Color transformations were done via observations of standard Landolt fields.

3. Source Detection and Count Rate

The discrete X-ray sources of the field were first found by running the CIAO wavelet algorithm *wavdetect* on an unbinned image of each chip. The source detection threshold was set to 5×10^{-7} , implying that a maximum of one false source would be detected within each chip. A total of 68 sources were then found: 7 sources in ACIS-I0, 19 sources in ACIS-I1, 16 sources in ACIS-I2, 23 sources in ACIS-I3 and 3 sources in ACIS-S3. As *wavdetect* is not 100% reliable, a second source detection was also performed. Using statistical thresholds calculated after Gehrels (1986), this second algorithm starts by eliminating all potential point-like sources and iteratively calculates the source-free background which may vary across the field-of-view. Then, using these background value(s), the algorithm detects all events exceeding the given threshold (i.e. 3 sigma in our case), groups them into spatially independent sources (whose separations exceed $2 \times \text{FWHM}_{PSF}$), and finally, it calculates the centroids of the sources. We searched for significant events on separated soft, medium and hard energy-band images and this second algorithm found 13 additional sources. Five of these sources have less than 10 net photons, and may be spurious detections. We thus

decided to discard them. We present in Table 1 the coordinates of the 75 remaining sources, listed by increasing Right Ascension (RA). Fig. 1 shows the sources' positions on the ACIS-I chips.

Note that HD 5980 is designated Src 41 and that Src 44, belonging most probably to the extended emission, probably does not constitute in itself a distinct point source. One source, Src 31, was 'detected' in the emission associated with the NGC 346 cluster. This emission was analysed in paper I and we won't repeat the discussion here. Some other sources are situated near a CCD gap and their derived properties should therefore be treated with caution.

Table 1 also lists the count rates of each source in the 0.3 – 10.0 keV energy band. The count rates were derived using the tool *dmextract*, from a spatial extraction of counts within a disk centered on the detected source and of radius varying from 2.5'' to 15'', depending of the off-axis angle. The background was extracted in an annulus directly surrounding the source, with the outer radius varying between 5'' and 22''. The analysis of the ACIS-S sources was more difficult due to the high background noise of these CCDs and the poor resolution this far off-axis. *wavdetect* was particularly confused in this region. For example, it found two close sources at the position of Src 75, whereas there is actually only one source. The second algorithm did a better job, but since the derived properties of any source in this region will not be very reliable, we decide not to analyse further these ACIS-S sources. Note however that Src 73 seems to possess a close neighbor (although this one was not detected by the detection algorithms): a comparison with the PSF expected at this position on the ACIS-S detector confirms that it may not be a single source.

4. Hardness Ratios

The properties of the point sources have also been studied using their hardness ratios (HRs). As in Sarazin, Irwin, & Bregman (2001) and Blanton, Sarazin, & Irwin (2001), we have defined *S*, *M* and *H* as the count rates in the 0.3 – 1.0 keV, 1.0 – 2.0 keV and 2.0 – 10.0 keV en-

¹⁰The WFI is a joint project between the European Southern Observatory (ESO), the Max-Planck-Institut für Astronomie (MPI-A) in Heidelberg (Germany) and the Osservatorio Astronomico di Capodimonte (OAC) in Naples (Italy). For more details, see <http://www.ls.eso.org/lasilla/Telescopes/2p2T/E2p2M/WFI/>

ergy bands. We then used these data to compute two HRs: $H21$ is defined as $(M - S)/(M + S)$ and $H31$ as $(H - S)/(H + S)$. For the sources with more than 50 cts (i.e., a minimum count rate of 5×10^{-4} cts s $^{-1}$), the S , M and H count rates are listed with the corresponding HRs in Table 2. Fig. 3 shows $H31$ as a function of $H21$ for these sources. No supersoft source is present : the HRs extend mainly from (0,0) to (1,1), with a tight correlation between the two HRs. The rather high HRs of the sources in the NGC 346 field, as compared e.g. to NGC 4697 (Sarazin, Irwin, & Bregman 2001) and NGC 1553 (Blanton, Sarazin, & Irwin 2001), can be explained by the larger foreground absorbing column.

5. Spectral Fitting

We have extracted the spectra of the detected point sources using the CIAO tool *psextract*. Only sources with at least 150 cts were fully analysed. The spectra were binned to reach a minimum of 10 cts per bin. Models were fitted within XSPEC, and we used either a simple absorbed *mekal* model or an absorbed power-law model, whose properties are summarized in Table 3. Unfortunately, the low Signal-to-Noise of most spectra did not allow us to discriminate between the models, so we have listed the parameters of both models, except if they give unphysical results (e.g. $kT \gg 10$ keV) or a statistically poor fit to the data. If neither model fits the data, other models were tested, and we have listed the parameters of the best one. Unless otherwise stated, the abundances of the *mekal* models were always fixed to the SMC mean value, $0.1Z_{\odot}$.

5.1. Absorption Column

To better understand the spectral properties of the point sources, we have tried to estimate the absorption column, $N(H)$. We can use two different ways. First, HI surveys provide us direct estimations of the hydrogen column: Schwering & Israel (1991) gives 4.3×10^{20} cm $^{-2}$ for the Galactic $N(HI)$ in the direction of the SMC; McGee & Newton (1982) have measured neutral hydrogen columns in the range $(3.7 - 5.3) \times 10^{21}$ cm $^{-2}$ towards NGC 346 and Israel (1997) quotes

4.4×10^{21} cm $^{-2}$ for $N(H_2)$ towards NGC 346. The value of the absorbing column should then be $\sim N(HI)_{\text{gal}}$ for sources located in front of the SMC, $N(HI)_{\text{gal}} + N(HI)_{\text{NGC 346}} + 2N(H_2)_{\text{NGC 346}}$ for extragalactic sources, and intermediate values for sources within the SMC.

A second estimation of the extinction towards NGC 346 can be made using the reddening, $E(B - V)$. Massey, Parker & Garmany (1989) measured an average $E(B - V)_{\text{SMC+gal}}$ of 0.14 mag in the cluster, while Schwering & Israel (1991) estimate a Galactic contribution of 0.07 to 0.09 mag towards the SMC. We can convert these values to absorption columns using the gas-to-dust ratios. For the Galaxy, this ratio is estimated to be $[N(H)/E(B - V)]_{\text{gal}} = 5.8 \times 10^{21}$ cm $^{-2}$ mag $^{-1}$ (Bohlin, Savage, & Drake 1978). For the SMC, the quoted values are in the range $[N(H)/E(B - V)]_{\text{SMC}} = (3.7 - 8.7) \times 10^{22}$ cm $^{-2}$ mag $^{-1}$ (Bouchet et al. 1985; Lequeux et al. 1994; Fitzpatrick 1985). A range of typical absorption columns towards NGC 346 can then be calculated using the expression

$$\left(\left[\frac{N(H)}{E(B-V)} \right]_{\text{gal}} E(B - V)_{\text{gal}} + \left[\frac{N(H)}{E(B-V)} \right]_{\text{SMC}} E(B - V)_{346} \right).$$

We can thus conclude that an absorption column in the $4 - 20 \times 10^{20}$ cm $^{-2}$ range indicates most probably a source in front of NGC 346 but still belonging to the SMC, while a column in the $2 - 6 \times 10^{21}$ cm $^{-2}$ is characteristic of a source situated in the NGC 346 cluster. A column higher than $\sim 10^{22}$ cm $^{-2}$ rather suggests an extragalactic source. A histogram of the values of the absorbing columns found in our spectral fits is presented in Fig. 4. It shows that most sources are indeed situated in NGC 346, with only few foreground sources and extragalactic sources.

6. Point Source Luminosity Function

We have used the X-ray luminosities of all the point sources detected in the field to construct a luminosity function, which can be compared to the overall luminosity function of the SMC, as well as to other galaxies. We thus first need to estimate the luminosities of the fainter sources on the basis of their count rate only.

To determine the countrate-to-luminosity conversion, we have assumed that all sources lie in the SMC, at a distance of 59 kpc. We further assumed that the data could be well represented by a power law of $\Gamma=1.6$. For the absorbing column, we chose $N(\text{H}) = 4 \times 10^{21} \text{ cm}^{-2}$, an average of that estimated for sources belonging to the cluster in § 5.1. Note that this arbitrary model appears consistent with a combined spectrum of all sources. For these parameters, *PIMMS*¹¹ gave us a typical absorbed flux of $1.4 \times 10^{-11} \text{ erg cm}^{-2} \text{ s}^{-1}$ for 1 cts s^{-1} in the 0.3 – 10.0 keV energy band. This leads to a countrate-to-absorbed-luminosity conversion factor of $5.7 \times 10^{36} \text{ erg cts}^{-1}$ (or $7.7 \times 10^{36} \text{ erg cts}^{-1}$ to get unabsorbed luminosities). The derived absorbed luminosities for the sources with <150 cts are listed in Table 1.

Using this conversion factor, we also derived the unabsorbed luminosities of all sources, including these with known spectral fits, and we constructed the cumulative distribution of the sources as a function of the X-ray luminosity (see Fig. 5). The best fit power law to our data, using a maximum likelihood minimisation algorithm (bayes in Sherpa v 2.3), has an exponent of -0.84 (with a 90% confidence range of -0.77 to -1.32). If we restrict the fit to the brightest luminosities ($\log[L_X^{\text{unabs}}] > 33.5$) - since they are less likely to be affected by incompleteness - , the slope is slightly steeper, -0.95 . However, a broken power-law provides a much better fit to the data. Its best fit slopes are -0.431 for $\log[L_X^{\text{unabs}}] < 33.68$ and -1.06 for $\log[L_X^{\text{unabs}}] > 33.68$ (with 90% confidence ranges of -0.42 to -0.44 , -0.95 to -1.18 , and 33.60 to 33.77 for the two slopes and the break point, respectively). Note that a fit using the unabsorbed luminosities from the spectral analysis for the brightest sources (see Table 3) gave very similar results.

For comparison, Bauer et al. (2001) indicate that the typical trend of the luminosity function for the SMC, M82 and NGC 3256 (all of which are star-forming galaxies of varying size) is $N \propto L_X^{-0.65}$ for $L_X > 10^{35} \text{ erg s}^{-1}$. The fit suggests that our data present a steeper slope than is seen for the entire SMC at higher luminosities,

and also for other star-forming galaxies. But note that our observations are sampling a lower luminosity range than in the other quoted examples. In addition, our luminosity function seems actually rather complex. It presents a rather flat profile at low luminosities. The function then steepens for $L_X^{\text{unabs}} > 33.7$ and flattens again for the highest luminosities ($L_X^{\text{unabs}} > 34.5$).

7. Source Identification

7.1. Comparison with Previous X-ray Observations

We have compared our source list to the *ROSAT* catalogs of SMC X-ray sources. Only 15 of the 75 sources were previously detected. We give in Table 4 the correspondence between our sources and those previously detected (Haberl et al. 2000). To be complete, we also quoted in this table the separation between our source and the *ROSAT* detections, and the 90% confidence error on the position given in the catalog of Haberl et al. (2000).

Of these 15 sources, Src 10, 20, 69, 70, 71, 72 and 74 fall slightly beyond the allowed range of RA and DEC of their *ROSAT* counterpart¹². Either the quoted errors were underestimated, or there are seven pairs of close transient sources in the field, with one member in a high state and the other in a quiescent state when the *ROSAT* observation was taken, and then exactly the reverse situation when *Chandra* took our data. As this possibility is very unlikely, we prefer to accept the identification with the quoted *ROSAT* sources.

During this comparison, we also found that one previously detected source was clearly missing: [HFP2000] 186 (Haberl et al. 2000). [HFP2000] 186 (quoted in *Simbad* with an O7III counterpart even if it is very close to a B-type star, AzV 219¹³), is not far from our Src 36, but still at a separation of $56''$, to be compared with the quoted positional error on this *ROSAT* source, $22''$. This source may be a transient X-ray binary (XRB). Three

¹¹available on <http://cxc.harvard.edu/toolkit/pimms.jsp>

¹²This is also true for the *ROSAT* sources observed on ACIS-S, but as all parameters derived for these sources are highly uncertain, we will not argue this point further.

¹³AzV stars come from the catalog by Azzopardi, Vigneau, & Macquet (1975)

other *ROSAT* sources, [HFP2000] 202, [SHP2000] 61, and [SHP2000] 75 (Haberl et al. 2000; Sasaki, Haberl, & Pietsch 2000), should be present in the ACIS-S field, but are not clearly detected.

7.2. Optical Counterparts

To search for optical counterparts to the ACIS-I sources, we have used the *DSS*¹⁴ and *MACHO*¹⁵ databases. In addition, we have also compared the X-ray data to ground-based images taken with the Wide Field Imager (WFI). The limiting magnitudes are $R \sim 17.5$ mag for the *DSS*, 20–21 mag for *MACHO* and ~ 21 mag for WFI. Before the comparison with the WFI images, a global shift of 0.3 s in RA and 1.2'' in DEC was first applied to the coordinates of our sources, so that the position of HD 5980 coincides almost perfectly in both datasets.

Next we have defined an optical counterpart as a star lying less than 3'' away from the position of the X-ray source. The results of this search are listed in the last column of Table 1. 32 sources possess at least one counterpart within the chosen 3'' error circle, but some of these counterparts are faint and/or lie just at the 3'' border. On the basis of the crowdeness of the field, we estimate that $\sim 20\%$ of these identifications may be spurious detections. 15 other sources do not seem to present any counterpart in any of the datasets. The status of the rest of the sources is unclear: they present a faint counterpart in some of the optical images, but not in all of them, so we considered these identifications more dubious than the previous ones. In Table 5, we present the *UBVRI* photometry of the counterparts found in the WFI data, and their separation from the X-ray source (after that the first global shift has been applied, see above). Note that the photometry of stars with $V > 20$ mag is rather uncertain, and has only an indicative value. Fig. 6 shows the color-magnitude diagram of all the sources detected in NGC 346 by the WFI. The majority of the X-ray emitting sources with $V < 20$ mag are within the main sequence of NGC 346. A second group contains rather faint ($V > 17$ mag) and redder stars

which probably belongs to the SMC but are not physically associated with the cluster.

Only two counterparts in the field already have a spectral classification: HD 5980 and the star situated at the peak of the cluster's emission. An estimation of the spectral types of the other counterparts has been made using the WFI photometry, the calibration of Schmidt-Kaler (1982), a distance of 59 kpc and a mean reddening $E(B-V)$ of 0.14 mag (Massey, Parker & Garmany 1989). This evaluation is given in the last column of Table 5. The majority of these newly cataloged counterparts seem to present a B spectral type. This result is not totally surprising since (a) X-ray binaries containing a Be star are expected to be moderately strong X-ray sources and to be brighter than in the case of a 'normal' B-star companion, and (b) Maeder, Grebel, & Mermilliod (1999) showed that the fraction of Be to B-type stars increases when metallicity decreases. With its low metallicity, the SMC should thus present a large population of Be/X-ray binaries, compared e.g. to the Galaxy, as was already suggested by e.g. Haberl & Sasaki (2000). A large number of the X-ray sources in the field are then probably Be/X-ray binaries. However, accurate spectroscopic observations of these stars are needed to confirm the spectral types and firmly secure this conclusion.

Among the identified sources, the slightly extended X-ray source Src 2 corresponds in fact to a small group of stars, too close to each other to disentangle their individual X-ray emission. Src 4, 6, and 70 are known Be/X-ray binaries (Be/XRBs). We confirm here the previous identifications of Src 6 with [MA93] 1038¹⁶ (Haberl & Sasaki 2000) and Src 70 with a "15–16th magnitude star" (Kahabka & Pietsch 1996). Haberl & Sasaki (2000) found another Be/XRB candidate in our field: [HFP2000] 170 (our Src 4). It lies between the emission-line stars AzV 191 and [MA93] 1016. The precise position of this source on the *ROSAT* observations made the association with either star unlikely, and we found that this source correlates well with a faint star situated between these two

¹⁴<http://archive.stsci.edu/dss/index.html>

¹⁵<http://www.macho.mcmaster.ca/>

¹⁶[MA93] stars come from the catalog by Meyssonnier & Azopardi (1993)

bright emission-line stars.

8. Source Variability

8.1. Short-Term Variability

We have searched for short-term X-ray variability in the lightcurves of the brightest point sources (with > 50 cts). Using a Kolmogorov-Smirnov test, we found that all lightcurves are consistent with a constant flux at the 95 % confidence level. However, KS tests are not very sensitive, so we have also checked the constancy using a χ^2 test. We have also compared the χ^2 of a constant fit with the χ^2 of a linear fit, to search for any improvement when using a linear fit. With these tests, we have detected a significant variability for Src 4, 6, and 41 (=HD 5980, see paper I). Figs. 7a and b show the lightcurves of Src 4 and 6, respectively. Src 4 and 41 present an increase of the count rate towards the end of the exposure, but the variability of Src 6 seems more complex and may be related to the Be phenomenon (see § 7.2).

Considering even higher frequency variability, Lamb et al. (2002) have detected a period of ~ 5 s in Src 69, the brightest point source of the field, which presents ~ 6000 cts in 100 ks. On the basis of its luminosity and its soft spectrum, they have proposed it to be an Anomalous X-ray Pulsar (AXP). Using our photometry, we have classified the counterpart as a probable early B star (see Table 5). This suggests that the source is in fact a Be/X-ray binary. From the P_{orb} vs P_{pulsar} diagram (Corbet 1986), we then derived an orbital period of ~ 25 d for this object.

8.2. Long-Term Variability

Long-term variations in the X-ray properties can also be checked by comparing our *Chandra* data to the *ROSAT* PSPC observations of the SMC. We have already mentioned (§ 7.1) at least one *ROSAT* source which was not detected in our *Chandra* observation. Such variations are indicative of transient sources.

One other transient source was already known in this field: Src 70. Kahabka & Pietsch (1996) reveal that this source is an X-ray binary evol-

ing from 1.3×10^{36} erg s $^{-1}$ in the high state to $< 4.6 \times 10^{34}$ erg s $^{-1}$ (i.e. undetected by *ROSAT*) six months later. In our dataset, this source is in the quiescent state, since its luminosity reaches only 2×10^{34} erg s $^{-1}$. We have used the *ROSAT* data to compare the spectral properties of this source during the high and low states. The best fit parameters to the *ROSAT* observation of Src 70 in the high state are: $N(H) = 0.39_{0.17}^{0.68} \times 10^{22}$ cm $^{-2}$ and $\Gamma = 2.82_{1.68}^{4.22}$. The flux in the 0.3 – 2.0 keV band was 5.03×10^{-13} erg cm $^{-2}$ s $^{-1}$ in October 1991, two orders of magnitude larger than the flux in the same band in May 2001 ($\sim 6 \times 10^{-15}$ erg cm $^{-2}$ s $^{-1}$). The variations of the spectrum of Src 70 can be seen in Fig. 8. Such luminosity variations were also observed in other sources, e.g. 2E0050.1 – 7247, but in this last case, the power-law steepened when the source luminosity decreased (Israel et al. 1997). However, if we consider only the *Chandra* data in the *ROSAT* energy range (0.3 – 2.0 keV), the fitted slopes of the power-laws are very similar in both datasets; thus we cannot conclude whether the power-law has steepened or not. This X-ray source also possesses a variable counterpart in the visible wavelengths. Fig. 9 shows the MACHO light curve of this counterpart in the blue and red filters, binned to 25 days. Both curves show a long-term increase, superposed on a sinusoidal variation with a period of ~ 1300 d. The properties of this interesting varying object are certainly worth further investigation.

We have compared *Chandra* and *ROSAT* data in the 0.3 – 2.0 keV range for the other bright sources detected by *ROSAT*. The spectral properties from the *ROSAT* data of these sources are compatible with the *Chandra* data within the error bars.

Finally, we note that some of the X-ray sources may possess a variable optical counterpart. From the MACHO database, we downloaded the red and blue lightcurves of the possible counterparts to our X-ray sources. Using a CLEANed algorithm (Roberts, Lehar, & Dreher 1987), we discovered that some of these sources correspond to long-term variables. They are presented in Table 6, along with the periods found (if any) and their MACHO id. Except for Src 70, no variation

was clearly detected for these sources in the X-ray domain, but future X-ray observations could provide additional checks.

9. Summary

In this series of articles, we report the analysis of the *Chandra* data of N66, the largest star formation region of the SMC. In this second article, we have focused on the other sources detected in the field. The X-ray properties of 75 point sources, of which 32 may possess an optical counterpart, have been analysed. Their cumulative luminosity function is steeper than the global one of the SMC at higher luminosities. Using new photometry of the NGC 346 field, we estimate that a large number of the counterparts are B-type stars, suggesting that many of the X-ray sources may be X-ray binaries. Considering their absorption column and the photometry of their counterparts, we also conclude that most of these X-ray sources probably belong to NGC 346. Finally, due to their variability, some of the objects should be monitored in the future, both in the visible and X-ray wavebands.

Support for this work was provided by the National Aeronautics and Space Administration through Chandra Award Number GO1-2013Z issued by the Chandra X-Ray Observatory Center, which is operated by the Smithsonian Astrophysical Observatory for and on behalf of NASA under contract NAS8-39073. Y.N. acknowledges support from the PRODEX XMM-OM and Integral Projects, contracts P4/05 and P5/36 ‘Pôle d’attraction Interuniversitaire (SSTC-Belgium) and from PPARC for an extended visit to the University of Birmingham. IRS and JMH also acknowledge support from PPARC. AFJM thanks NSERC (Canada) and FCAR (Quebec) for financial aid. This paper utilizes public domain data from the DSS, 2MASS, USNO, GSC, and the MACHO Project. This research has made use of the SIMBAD database, operated at CDS, Strasbourg, France and NASA’s Astrophysics Data System Abstract Service.

REFERENCES

- Arnaud, K. 1996, ASP Conf. Ser. 101, eds G. Jacoby & J. Barnes, p.17
- Azzopardi, M., Vigneau, J., & Macquet, M. 1975, A&AS, 22, 285 (AzV)
- Bauer, F.E., Brandt, W.N., Sambruna, R.M., Chartas, G., Garmire, G.P., Kaspi, S., & Netzer, H. 2001, AJ, 122, 182
- Blanton, E.L., Sarazin, C.L., & Irwin, J.A. 2001 ApJ, 552, 106
- Bohlin, R.C., Savage, B.D., & Drake, J.F. 1978, ApJ, 224, 132
- Bouchet, P., Lequeux, J., Maurice, E., Prevot, L., & Prevot-Burnichon, M.L. 1978, A&A, 149, 330
- Corbet, R.H.D. 1986, MNRAS, 220, 1047
- Fitzpatrick, E.L. 1985, ApJS, 59, 77
- Gehrels, N. 1986, ApJ, 303, 336
- Haberl, F., Filipovic, M. D., Pietsch, W., & Kahabka, P. 2000, A&AS, 142, 41 (HFP2000)
- Haberl, F., & Sasaki, M. 2000, A&A 359, 573
- Henize, K.G. 1956, ApJS, 2, 315
- Irwin, J.A., Sarazin, C.L., & Bregman, J.N. 2002, ApJ, submitted (astro-ph/0107493)
- Israel, G.L., Stella, L., Angelini, L., White, N.E., Giommi, P., & Covino, S. 1997, ApJ, 484, L141
- Israel, F.P. 1997, A&A, 328, 471
- Kahabka, P., & Pietsch, W. 1996, A&A, 312, 919
- Lamb, R.C., Fox, D.W., Macomb, D.J., & Prince, T.A. 2002, submitted (astro-ph/0205310)
- Lejeune, T. & Schaerer, D. 2001, A&A, 366, 538
- Lequeux, J., Le Bourlot, J., Des Forets, G.P., Roueff, E., Boulanger, F., & Rubio, M. 1994, A&A, 292, 371
- McGee, R.X. & Newton, L.M. 1982, PASA, 4, 308
- Maeder, A., Grebel, E.K., & Mermilliod, J.-C. 1999, A&A, 346, 459

- Martin C.L., Kobulnicky, H.A., & Heckman T.M. 2002, submitted (astro-ph/0203513)
- Mason, K.O., Breeveld, A., Much, R., Carter, M., Cordova, F.A., Cropper, M.S., Fordham, J., Huckle, H., Ho, C., Kawakami, H., Kennea, J., Kennedy, T., Mittaz, J., Pandel, D., Priedhorsky, W.C., Sasseen, T., Shirey, R., Smith, P., & Vreux, J.-M. 2001, A&A, 365, L36
- Massey, P., Parker, J.W., & Garmany, C.D. 1989, AJ, 98, 1305
- Mathewson, D.S., Ford, V.L., & Visvanathan, N. 1986, ApJ 301, 664
- Meyssonnier, N., & Azzopardi, M. 1993, A&AS, 102, 451 (MA93)
- Nazé Y., Hartwell, J.M., Stevens, I.R., Corcoran, M.F., Chu, Y.-H., Koenigsberger, G., Moffat, A.F.J., & Niemela, V.S. 2002, ApJ, in press (paper I)
- Roberts, D.H., Lehar, J., & Dreher, J.W. 1987, AJ, 93, 968
- Sarazin, C.L., Irwin, J.A., & Bregman, J.N. 2001, ApJ, 556, 533
- Sasaki, M., Haberl, F., & Pietsch, W. 2000, A&AS, 147, 75 (SHP2000)
- Schmidt-Kaler, T. 1982, Landölt-Bornstein Catalogue VI/2b
- Schwering, P.B.W. & Israel, F.P. 1991, A&A, 246, 231
- Ye, T., Turtle, A.J., & Kennicutt, R.C., Jr. 1991, MNRAS, 249, 722

Fig. 1.— *Chandra* ACIS-I color image of the NGC 346 cluster. Three energy bands were used to create this color image : red corresponds to 0.3-2.0 keV, green to 2.0-4.0 keV and blue to 4.0-10.0 keV. Before combination, the images were binned by a factor of two and smoothed by convolution with a gaussian of $\sigma=2''$. The identification numbers of the sources found in the ACIS-I data of NGC 346 are shown (see Table 1 for a list of positions). The NGC 346 cluster corresponds to Src 31 and HD 5980 is Src 41. A cross has been used to show the location of faint sources. Note that a number of point sources were located on the ACIS-S3 chip and are not shown in this diagram (Srcs 72 to 75 - see text for more details).

Fig. 2.— The *Chandra* X-ray data superposed on the *DSS* image of the field. The X-ray data were first binned by a factor of 4 and then smoothed by convolution with a gaussian of $\sigma = 4''$. Note that except for HD 5980 and the cluster, the brightest stars generally do not correspond to X-ray sources.

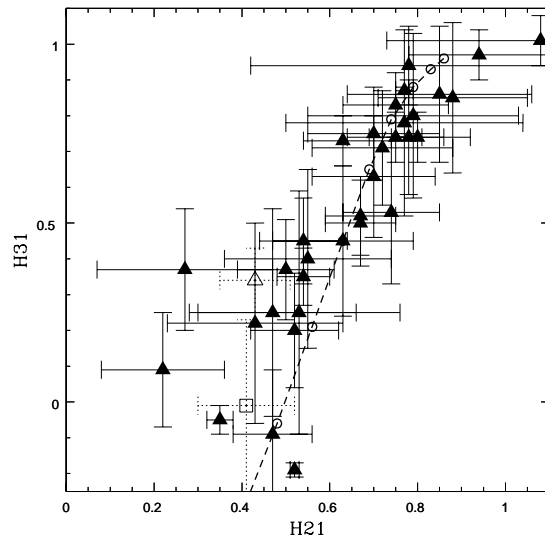


Fig. 3.— Hardness ratios of the brightest sources (those with a total of > 50 counts). The NGC 346 cluster is shown as an open square and HD 5980 as an open triangle. Errors bars correspond to \pm one standard deviation. The open circles connected by a dashed line represents the colors predicted using PIMMS for an absorbed power-law model with a column density of $4 \times 10^{21} \text{ cm}^{-2}$ (see § 6) and an exponent Γ varying from 0 (upper right) to 2.8 in increments of 0.4 (Irwin, Sarazin, & Bregman 2002). The extended emission surrounding HD 5980 is not shown on the diagram, being very soft, with $H21 = -0.24 \pm 0.02$ and $H31 = -0.96 \pm 0.05$.

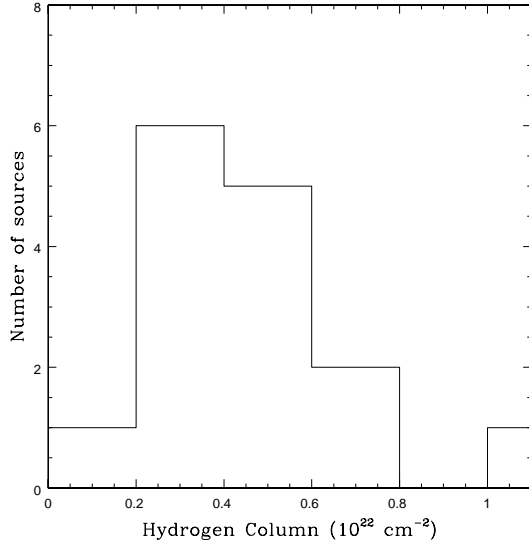


Fig. 4.— Histogram of the different values of the absorbing column $N(\text{H})$ found for the point sources from the spectral fitting. Sources with a column of $\sim 2 - 6 \times 10^{21} \text{ cm}^{-2}$ are probably associated with NGC 346, while those sources with $N(\text{H}) \geq 10^{22} \text{ cm}^{-2}$ are likely to be extragalactic in nature.

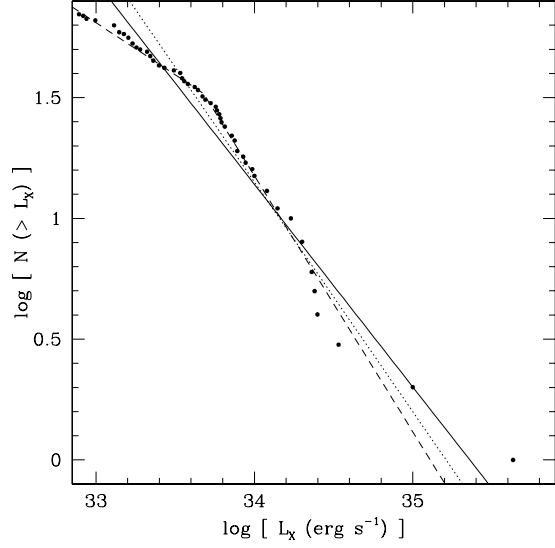


Fig. 5.— Histogram of the cumulative X-ray luminosity function of all the detected sources versus 0.3 – 10.0 keV unabsorbed luminosity. The continuous line is the best-fit power law to the data ($N \propto L_X^{-0.84}$), while the dotted line is the best-fit power law to the brightest data ($N \propto L_X^{-0.95}$ for $\log(L_X^{\text{unabs}}) > 33.5$). The dashed line presents the best-fit broken power law to the data, with slopes of -0.43 for $\log(L_X^{\text{unabs}}) < 33.7$ and -1.06 for $\log(L_X^{\text{unabs}}) > 33.7$.

Fig. 6.— The Color-Magnitude Diagram of NGC 346 using the WFI data. The sources listed in Table 5 are shown in red circles. The size of the circles is proportional to $\log(L_X^{\text{abs}})$ (see Table 1). The error bars correspond to the dispersion of the measured data (for some stars, the errors are smaller than the disk's size). Counterparts with $V > 20$ mag were not included since their photometry is very uncertain. The solid line shows an isochrone of 5 Myr for $Z=0.004$ (Lejeune & Schaerer 2001) transformed using a distance of 59 kpc and reddened with $R_V=3.3$ and $E(B-V)$ of 0.14 mag (Massey, Parker & Garmany 1989). Note that HD 5980 lies at the upper left of the diagram.

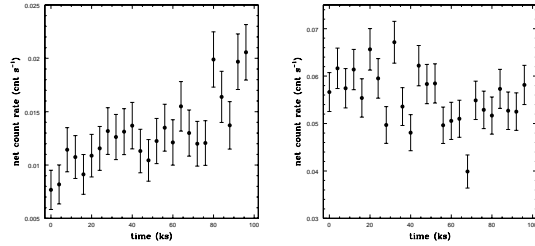


Fig. 7.— The *Chandra* X-ray lightcurves of the sources identified as being variable : Src 4 (a) and Src 6 (b). The lightcurves are in the 0.3-10 keV range and with 25 bins of 4 ks each. A third variable source, Src 41 (=HD 5980), has been discussed extensively in paper I. The error bars correspond to \pm one standard deviation.

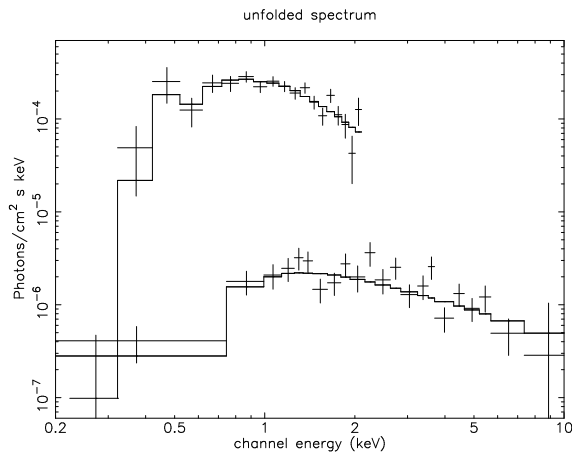


Fig. 8.— Variations of the (unfolded) spectrum of Src 70: *ROSAT* data (upper part) extend on a smaller energy range than *Chandra*'s (bottom part) but show a substantially increased luminosity. Horizontal errors bars correspond to the energy range covered by the bin and the vertical bars represent \pm one standard deviation. The presented models are absorbed power-laws with $N(\text{H})_{\text{ROSAT}} = 0.39 \times 10^{22} \text{ cm}^{-2}$, $\Gamma_{\text{ROSAT}}=2.82$, $N(\text{H})_{\text{Chandra}} = 0.36 \times 10^{22} \text{ cm}^{-2}$, $\Gamma_{\text{Chandra}}=1.01$.

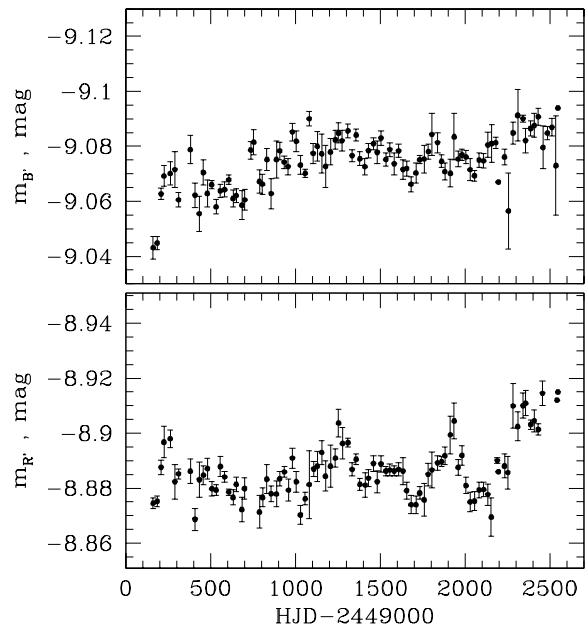


Fig. 9.— MACHO light curve of the optical counterpart to Src 70 in the blue and red filters, binned to 25 d. The last MACHO data were taken \sim 500 d before the *Chandra* observation. Error bars correspond to the dispersion of the measured magnitudes in each bin.

Table 1: Coordinates of all detected sources with their individual count rate and absorbed luminosities in the 0.3–10.0 keV band (see § 6). All errors represent \pm one standard deviation, with the errors on the coordinates given in s for the right ascension (RA) and in " for the declination (DEC). The last two columns indicate if the source is variable (see § 8) and if it possesses an optical counterpart (see § 7.2). A counterpart is defined as lying within $\sim 3''$ from the central position of the X-ray source. A '?' status was attributed when a faint counterpart was detected at the position, but only in one of the datasets.

Src	RA (2000) <i>hh mm ss \pm ss</i>	DEC (2000) <i>° ' " \pm "</i>	Count Rate 10^{-4} cts s $^{-1}$	L_X^{abs} 10^{33} erg s $^{-1}$	Var. ?	C.part ?
1	00 56 52.178 \pm 0.037	−72 12 03.80 \pm 0.25	26.5 \pm 2.2	16.9 ^a	N	?
2	00 57 12.904 \pm 0.048	−72 10 43.25 \pm 0.19	8.41 \pm 1.18	4.83	N	Y
3	00 57 30.060 \pm 0.070	−72 10 09.20 \pm 0.32	2.93 \pm 0.90	1.68		?
4	00 57 32.411 \pm 0.012	−72 13 01.41 \pm 0.06	131 \pm 4	44.1 ^a	Y	Y
5	00 57 41.568 \pm 0.043	−72 09 02.59 \pm 0.23	7.57 \pm 1.17	4.35	N	?
6	00 57 50.041 \pm 0.004	−72 07 54.96 \pm 0.03	560 \pm 8	538. ^a	Y	Y
7	00 57 51.162 \pm 0.055	−72 08 27.75 \pm 0.39	2.13 \pm 0.71	1.22		N
8	00 57 59.561 \pm 0.071	−72 16 19.18 \pm 0.23	6.36 \pm 1.14	3.65	N	?
9	00 58 00.323 \pm 0.041	−72 08 22.01 \pm 0.22	2.77 \pm 0.70	1.59		Y
10	00 58 02.309 \pm 0.031	−72 12 05.68 \pm 0.13	15.7 \pm 1.5	10.0 ^a	N	?
11	00 58 07.265 \pm 0.073	−72 13 48.43 \pm 0.23	1.76 \pm 0.66	1.01		Y
12	00 58 08.409 \pm 0.047	−72 03 36.98 \pm 0.33	8.01 \pm 1.23	4.60	N	N
13	00 58 09.066 \pm 0.022	−72 08 25.62 \pm 0.15	10.1 \pm 1.2	5.80	?	N
14	00 58 09.370 \pm 0.070	−72 16 12.20 \pm 0.32	4.66 \pm 1.22	2.68		N
15	00 58 11.883 \pm 0.052	−72 07 18.94 \pm 0.41	2.34 \pm 0.69	1.34		?
16	00 58 19.900 \pm 0.070	−72 16 17.80 \pm 0.32	1.76 \pm 0.76	1.01		Y
17	00 58 22.688 \pm 0.042	−72 14 48.48 \pm 0.31	1.65 \pm 0.68	0.95		?
18	00 58 27.126 \pm 0.019	−72 10 24.68 \pm 0.16	3.24 \pm 0.71	1.86		N
19	00 58 27.453 \pm 0.027	−72 04 57.36 \pm 0.17	15.7 \pm 1.5	9.55 ^a	N	N
20	00 58 30.043 \pm 0.011	−72 08 39.98 \pm 0.05	22.3 \pm 1.7	9.60 ^a	N	Y
21	00 58 30.370 \pm 0.070	−72 00 44.60 \pm 0.32	6.80 \pm 1.25	3.90	N	N
22	00 58 30.687 \pm 0.039	−72 15 28.36 \pm 0.18	5.44 \pm 0.98	3.12		Y
23	00 58 31.478 \pm 0.024	−72 09 50.62 \pm 0.10	4.49 \pm 0.79	2.58		?
24	00 58 37.336 \pm 0.020	−72 03 21.95 \pm 0.11	43.4 \pm 2.3	22.7 ^a	N	?
25	00 58 37.753 \pm 0.071	−72 14 35.71 \pm 0.23	2.48 \pm 0.78	1.42		N
26	00 58 39.386 \pm 0.034	−72 02 27.15 \pm 0.27	10.2 \pm 1.3	5.86	N	?
27	00 58 49.750 \pm 0.070	−72 17 14.90 \pm 0.32	2.99 \pm 0.98	1.72		Y
28	00 58 58.200 \pm 0.070	−72 01 07.40 \pm 0.32	1.08 \pm 0.69	0.62		Y
29	00 59 00.744 \pm 0.008	−72 13 28.75 \pm 0.04	31.8 \pm 1.9	18.5 ^a	N	Y
30	00 59 03.105 \pm 0.007	−72 12 22.80 \pm 0.03	30.6 \pm 1.9	14.6 ^a	N	N
31	00 59 04.165 \pm 0.039	−72 10 23.25 \pm 0.15	in the cluster's core, see paper I			Y
32	00 59 08.135 \pm 0.020	−72 12 45.85 \pm 0.10	1.12 \pm 0.47	0.64		?
33	00 59 08.915 \pm 0.084	−72 15 31.01 \pm 0.22	1.72 \pm 0.65	0.99		?
34	00 59 11.273 \pm 0.041	−72 12 23.61 \pm 0.16	1.01 \pm 0.50	0.58		?

Table 1: (continued)

35	00 59	12.490±0.070	−72 20	11.70±0.32	4.36±1.06	2.50		Y
36	00 59	13.042±0.045	−72 16	17.80±0.12	11.4±1.3	6.54	N	Y
37	00 59	18.146±0.024	−72 11	14.90±0.10	2.84±0.70	1.63		?
38	00 59	18.826±0.041	−72 04	23.55±0.26	7.33±1.10	4.21	N	Y
39	00 59	21.780±0.050	−72 15	40.12±0.19	2.37±0.68	1.36		Y
40	00 59	25.365±0.039	−72 14	31.47±0.12	7.93±1.04	4.55	N	?
41	00 59	26.247±0.010	−72 09	52.66±0.04	29.8±1.9	13.3 ^a	Y	Y
42	00 59	29.589±0.034	−72 12	34.65±0.17	1.12±0.47	0.64		?
43	00 59	31.434±0.024	−72 14	17.24±0.11	13.4±1.3	7.69	N	?
44	00 59	33.762±0.042	−72 10	39.72±0.19	3.20±1.24	1.84		N
45	00 59	33.972±0.018	−72 07	48.36±0.09	9.77±1.16	5.61	N	Y
46	00 59	34.776±0.038	−72 02	10.73±0.20	17.9±1.7	6.95 ^a	N	Y
47	00 59	35.223±0.022	−72 08	35.08±0.10	3.99±0.79	2.29		?
48	00 59	36.925±0.068	−72 16	52.46±0.17	5.67±1.06	3.25	N	Y
49	00 59	40.232±0.075	−72 19	03.24±0.15	11.0±1.4	6.31	N	?
50	00 59	42.910±0.045	−72 13	06.94±0.15	2.06±0.73	1.18		Y
51	00 59	46.214±0.048	−72 02	51.73±0.33	6.13±1.10	3.52	N	N
52	00 59	47.340±0.027	−72 09	29.51±0.12	2.16±0.62	1.24		?
53	00 59	49.632±0.044	−72 10	20.14±0.21	1.93±0.62	1.11		Y
54	00 59	52.006±0.064	−72 16	40.39±0.33	1.69±0.69	0.97		N
55	00 59	52.542±0.051	−72 15	30.39±0.14	9.32±1.14	5.35	N	?
56	00 59	53.254±0.054	−72 06	34.00±0.21	4.49±0.87	2.58		Y
57	00 59	54.300±0.048	−72 10	31.79±0.18	1.82±0.62	1.04		Y
58	01 00	06.170±0.070	−72 13	44.00±0.32	1.28±0.64	0.73		N
59	01 00	11.742±0.087	−72 16	29.06±0.21	2.84±0.83	1.63		Y
60	01 00	15.509±0.036	−72 04	41.21±0.17	26.4±2.0	12.1 ^a	?	Y
61	01 00	17.138±0.053	−72 10	50.07±0.20	4.91±0.89	2.81		Y
62	01 00	22.994±0.033	−72 11	28.73±0.15	12.6±1.4	7.23	?	N
63	01 00	28.081±0.055	−72 05	33.30±0.22	7.73±1.43	4.44	N	?
64	01 00	28.460±0.070	−72 04	51.50±0.32	2.25±0.83	1.29		?
65	01 00	29.039±0.055	−72 05	12.33±0.26	6.03±1.33	3.46	N	Y
66	01 00	30.126±0.071	−72 11	29.14±0.18	2.23±0.66	1.28		N
67	01 00	36.740±0.070	−72 09	13.60±0.32	3.45±0.87	1.98		?
68	01 00	36.919±0.058	−72 13	16.33±0.20	9.32±1.29	5.35	?	Y
69	01 00	42.828±0.007	−72 11	32.36±0.02	606±8	150. ^a	N	Y
70	01 01	02.620±0.041	−72 06	57.54±0.19	29.2±2.0	25.5 ^a	Y	Y
71	01 01	03.898±0.046	−72 10	04.96±0.16	18.0±1.6	5.25 ^a	N	Y
72	00 56	42.10±0.24	−72 20	27.4±1.1	see §3			
73	00 57	18.70±0.12	−72 25	30.3±1.5	see §3			
74	00 57	24.61±0.12	−72 23	58.5±1.0	see §3			
75	00 57	35.23±0.28	−72 19	30.7±2.7	see §3			

^aThis luminosity is an average of the luminosities from the models of Table 3.

Table 2: Count rates in the 0.3-1.0 keV (S), 1.0-2.0 keV (M) and 2.0-10.0 keV (H) energy bands, and derived hardness ratios for the brightest sources (> 50 cts). $H21$ is defined as $(M - S)/(M + S)$ and $H31$ as $(H - S)/(H + S)$. Stated errors correspond to \pm one standard deviation.

Src	S 10^{-4} cts s $^{-1}$	M 10^{-4} cts s $^{-1}$	H 10^{-4} cts s $^{-1}$	$H21$	$H31$
1	3.81 \pm 0.99	12.6 \pm 1.4	10.0 \pm 1.5	0.54 \pm 0.10	0.45 \pm 0.12
2	1.72 \pm 0.58	2.97 \pm 0.75	3.72 \pm 0.83	0.27 \pm 0.20	0.37 \pm 0.17
4	32.7 \pm 2.0	68.5 \pm 2.8	29.5 \pm 1.9	0.35 \pm 0.03	-0.05 \pm 0.04
5	1.11 \pm 0.57	3.87 \pm 0.78	2.59 \pm 0.82	0.55 \pm 0.19	0.40 \pm 0.25
6	23.9 \pm 1.7	187 \pm 4	350 \pm 6	0.77 \pm 0.02	0.87 \pm 0.01
8	1.17 \pm 0.52	3.25 \pm 0.75	1.94 \pm 0.84	0.47 \pm 0.19	0.25 \pm 0.29
10	2.54 \pm 0.69	7.55 \pm 1.01	5.57 \pm 0.97	0.50 \pm 0.11	0.37 \pm 0.14
12	0.27 \pm 0.42	4.29 \pm 0.81	3.45 \pm 0.94	0.88 \pm 0.17	0.85 \pm 0.21
13	0.91 \pm 0.45	6.18 \pm 0.90	2.97 \pm 0.71	0.74 \pm 0.11	0.53 \pm 0.20
19	0.83 \pm 0.45	5.86 \pm 0.90	9.04 \pm 1.15	0.75 \pm 0.12	0.83 \pm 0.09
20	2.43 \pm 0.64	12.1 \pm 1.2	7.75 \pm 1.04	0.67 \pm 0.08	0.52 \pm 0.11
21	1.34 \pm 0.55	3.37 \pm 0.85	2.09 \pm 0.87	0.43 \pm 0.20	0.22 \pm 0.28
24	6.69 \pm 1.01	22.7 \pm 1.7	14.0 \pm 1.5	0.54 \pm 0.06	0.35 \pm 0.08
26	0.77 \pm 0.49	4.78 \pm 0.85	4.63 \pm 0.94	0.72 \pm 0.16	0.71 \pm 0.16
29	2.13 \pm 0.59	15.2 \pm 1.4	14.4 \pm 1.3	0.75 \pm 0.06	0.74 \pm 0.07
30	1.82 \pm 0.54	16.7 \pm 1.4	12.1 \pm 1.2	0.80 \pm 0.06	0.74 \pm 0.07
36	0.84 \pm 0.47	4.73 \pm 0.85	5.84 \pm 0.93	0.70 \pm 0.15	0.75 \pm 0.13
38	0.27 \pm 0.40	3.33 \pm 0.71	3.73 \pm 0.86	0.85 \pm 0.21	0.86 \pm 0.19
40	0.99 \pm 0.48	4.30 \pm 0.78	2.64 \pm 0.65	0.63 \pm 0.16	0.45 \pm 0.21
41	5.34 \pm 0.90	13.5 \pm 1.3	10.9 \pm 1.2	0.43 \pm 0.08	0.34 \pm 0.09
43	0.13 \pm 0.34	4.14 \pm 0.78	9.10 \pm 1.13	0.94 \pm 0.16	0.97 \pm 0.07
45	-0.06 \pm 0.27	1.64 \pm 0.54	8.19 \pm 1.06	1.08 \pm 0.35	1.01 \pm 0.07
46	3.14 \pm 0.76	10.0 \pm 1.2	4.73 \pm 1.05	0.52 \pm 0.10	0.20 \pm 0.16
48	0.95 \pm 0.56	3.12 \pm 0.71	1.60 \pm 0.71	0.53 \pm 0.23	0.25 \pm 0.34
49	0.71 \pm 0.48	5.61 \pm 0.92	4.70 \pm 1.02	0.78 \pm 0.14	0.74 \pm 0.16
51	0.33 \pm 0.42	2.81 \pm 0.73	2.98 \pm 0.84	0.79 \pm 0.24	0.80 \pm 0.23
55	0.84 \pm 0.45	4.73 \pm 0.82	3.75 \pm 0.78	0.70 \pm 0.14	0.63 \pm 0.17
60	2.92 \pm 0.84	14.8 \pm 1.4	8.75 \pm 1.38	0.67 \pm 0.08	0.50 \pm 0.12
62	3.36 \pm 0.79	5.28 \pm 0.89	4.00 \pm 0.94	0.22 \pm 0.14	0.09 \pm 0.16
63	0.46 \pm 0.60	3.51 \pm 0.84	3.76 \pm 1.14	0.77 \pm 0.27	0.78 \pm 0.26
65	-0.57 \pm 0.55	3.81 \pm 0.87	2.80 \pm 1.00	1.35 \pm 0.41	1.51 \pm 0.66
68	0.24 \pm 0.42	1.89 \pm 0.64	7.20 \pm 1.13	0.78 \pm 0.36	0.94 \pm 0.11
69	124 \pm 4	398 \pm 6	83.6 \pm 3.1	0.52 \pm 0.01	-0.19 \pm 0.02
70	2.50 \pm 0.72	10.9 \pm 1.2	15.8 \pm 1.5	0.63 \pm 0.09	0.73 \pm 0.07
71	3.88 \pm 0.81	10.9 \pm 1.2	3.24 \pm 0.92	0.47 \pm 0.09	-0.09 \pm 0.18

Table 3: Parameters of the spectral fits for the sources with at least 150 cts. Stated errors correspond to the 90 % confidence level. Abundances are fixed at $0.1 Z_{\odot}$, except for src 69, where the best fit is found for $Z = 0.0022^{+0.0094}_{-0.0001} Z_{\odot}$. Absorbed luminosities are given in the spectral range $0.3 - 10$ keV and for a distance of 59 kpc.

Src	Model	L_X^{abs} $10^{34} \text{ ergs s}^{-1}$	χ^2_{ν}	$N(\text{H})$ 10^{22} cm^{-2}	Other Parameters (kT in keV)	N_{dof}
1	wabs*mekal	1.65	0.81	$0.29^{+0.49}_{-0.15}$	$kT = 9.37^{+55.75}_{-4.56}$	29
	wabs*pow	1.72	0.82	$0.36^{+0.57}_{-0.21}$	$\Gamma = 1.65^{+1.98}_{-1.32}$	29
4	wabs*mekal	4.26	1.19	$0.17^{+0.19}_{-0.13}$	$kT = 2.87^{+3.60}_{-2.50}$	97
	wabs*pow	4.55	1.06	$0.29^{+0.32}_{-0.24}$	$\Gamma = 2.36^{+2.51}_{-2.20}$	97
6	wabs*pow	55.0	1.57	$0.51^{+0.56}_{-0.45}$	$\Gamma = 0.86^{+0.93}_{-0.80}$	317
	wabs*(mekal+ wabs*pow)	52.5	1.52	$1.02^{+1.20}_{-0.89}$	$kT = 0.58^{+0.65}_{-0.49} N_{H2} = 0.87^{+1.64}_{-0.17}$	314
10	wabs*pow	1.00	0.91	$0.16^{+0.34}_{-0.04}$	$\Gamma = 1.50^{+1.94}_{-1.18}$	14
19	wabs*mekal	0.95	1.86	$1.39^{+2.13}_{-0.74}$	$kT = 5.52^{+100.00}_{-2.04}$	14
	wabs*pow	0.96	1.78	$1.80^{+2.89}_{-0.87}$	$\Gamma = 2.21^{+3.16}_{-1.68}$	14
20	wabs*mekal	0.92	0.30	$0.50^{+0.65}_{-0.35}$	$kT = 3.68^{+6.60}_{-2.57}$	19
	wabs*pow	1.00	0.24	$0.64^{+0.91}_{-0.48}$	$\Gamma = 2.18^{+2.40}_{-1.85}$	19
24	wabs*mekal	2.22	1.10	$0.19^{+0.27}_{-0.12}$	$kT = 7.43^{+16.60}_{-4.52}$	39
	wabs*pow	2.32	1.06	$0.26^{+0.36}_{-0.19}$	$\Gamma = 1.75^{+1.92}_{-1.52}$	39
29	wabs*pow	1.85	0.94	$0.54^{+0.73}_{-0.39}$	$\Gamma = 1.64^{+1.86}_{-1.38}$	29
30	wabs*mekal	1.42	0.61	$0.57^{+0.74}_{-0.44}$	$kT = 4.24^{+6.66}_{-3.63}$	25
	wabs*pow	1.50	0.61	$0.74^{+0.95}_{-0.57}$	$\Gamma = 2.16^{+2.30}_{-1.82}$	25
41	wabs*mekal	1.30	1.24	$0.22^{+0.35}_{-0.14}$	$kT = 7.04^{+13.35}_{-4.35}$	27
	wabs*pow	1.36	1.30	$0.28^{+0.44}_{-0.19}$	$\Gamma = 1.74^{+1.89}_{-1.53}$	27
46	wabs*mekal	0.67	1.26	$0.39^{+0.58}_{-0.26}$	$kT = 2.60^{+4.47}_{-1.29}$	17
	wabs*pow	0.72	1.23	$0.56^{+0.82}_{-0.41}$	$\Gamma = 2.51^{+3.10}_{-2.09}$	17
60	wabs*mekal	1.15	0.81	$0.40^{+0.58}_{-0.33}$	$kT = 4.06^{+8.63}_{-2.46}$	27
	wabs*pow	1.27	0.78	$0.51^{+0.77}_{-0.35}$	$\Gamma = 2.05^{+2.46}_{-1.71}$	27
69 ^a	wabs*mekal	14.9	1.42	$0.41^{+0.44}_{-0.38}$	$kT = 1.04^{+1.11}_{-0.99}$	163
	wabs*pow	15.1	1.75	$0.71^{+0.75}_{-0.67}$	$\Gamma = 3.82^{+3.93}_{-3.71}$	164
70	wabs*pow	2.55	1.13	$0.36^{+0.63}_{-0.20}$	$\Gamma = 1.01^{+1.32}_{-0.76}$	29
71	wabs*mekal	0.51	1.45	$0.25^{+0.50}_{-0.15}$	$kT = 1.91^{+3.12}_{-0.99}$	16
	wabs*pow	0.54	1.27	$0.47^{+0.82}_{-0.30}$	$\Gamma = 2.93^{+3.31}_{-2.44}$	16

^a $Z = 0.0022^{+0.0094}_{-0.0001} Z_{\odot}$

Table 4: X-ray sources previously detected by ROSAT in the NGC 346 field. The ids and positions of the [HFP2000] sources are taken from Haberl et al. (2000). The last columns list the positional error of the ROSAT sources (from Haberl et al. 2000), and the separation between *Chandra* and ROSAT sources.

Src	[HFP2000]	RA (2000) <i>hh mm ss</i>	DEC (2000) <i>° ' "</i>	Pos. Er. <i>"</i>	Sep. <i>"</i>
1	164	00 56 52.4	−72 12 00	9.8	3.9
4	170	00 57 31.8	−72 13 03	3.6	3.2
6	136	00 57 50.1	−72 07 56	5.1	1.1
10	165	00 58 00.8	−72 12 09	6.3	7.7
11	173	00 58 01.7	−72 13 51	28.2	25.6
16	185	00 58 16.3	−72 16 18	19.0	16.4
20	139	00 58 28.1	−72 08 48	11.0	12.0
24	116	00 58 35.2	−72 03 12	19.4	14.0
60	123	01 00 13.1	−72 04 40	15.9	11.2
69	162	01 00 41.5	−72 11 34	2.3	6.3
70	132	01 01 01.1	−72 06 57	2.8	7.0
71	150	01 01 07.9	−72 10 26	19.0	27.9
72	206	00 56 39.8	−72 20 28	7.4	10.5
73	234	00 57 18.9	−72 25 30	3.4	1.0
74	223	00 57 21.9	−72 23 57	11.6	12.4

Table 5: Photometry of the optical counterparts (WFI data), and separation between the X-ray source and its counterpart. The error quoted in the σ_V column represents the dispersion of the measured data. A ‘:’ denotes an uncertain value. If the counterpart is cataloged, the identifier is given in the last column of the Table, together with its spectral type in parentheses, if known. Identifiers beginning by ‘S010202’ are taken from the Guide Star Catalog-II. When it was possible, an estimation of the spectral type of the source was made, assuming that it belongs to NGC 346 ($E(B - V)=0.14$ mag, $d=59$ kpc). The result is written in italics in the last column.

Src	V (mag)	$B - V$ (mag)	$U - B$ (mag)	$V - R$ (mag)	$R - I$ (mag)	$V - I$ (mag)	σ_V (mag)	Sep. (")	Remarks
1	21.32	0.55		0.43	2.14	2.57	0.14	1.6	<i>F5III</i>
2 ^a	17.14	0.54		0.53	0.29	0.82	0.02	2.2	S010202097601, USNO-A2.0 0150-00623029
3	19.67	-0.01		-0.08	-0.22	-0.30	0.01	0.9	<i>B9V</i> , S0102029846
4	18.19	0.50		0.16			0.05	0.9	S01020206684, USNO-A2.0 0150-00629718
6	15.71	0.01	-0.96	0.10	0.05	0.14	0.01	0.5	[MA93]1038 ^b <i>late O, early B star</i>
9	18.86	-0.12	-0.49	0.09			0.09	1.1	<i>B6V</i> , S010202012821, USNO-A2.0 0150-00638074
10	17.57	-0.04	-0.72	-0.10			0.02	1.8	<i>B2-3V</i> , S0102027728
11 ^c	19.11	0.25		0.62	1.46	2.08	0.04	1.3	S01020205791, 2MASS 0058077-721349
16	20.70	-0.12		-0.31			0.05	0.2	
20	20.88:	1.28:		1.15:	0.86:	2.01:	0.27	0.7	
22	19.25	-0.16	-0.36	-0.13	1.00	0.87	0.10	0.7	
26	20.05	-0.08		-0.24			0.04	0.1	
28	18.71	1.49		0.95	1.37	2.33	0.06	2.5	<i>K4III</i> , S010202028457
29	19.41	0.16				0.53	0.08	1.7	<i>A1III</i>
31	12.61	-0.15	-1.07	-0.06	-0.18	-0.24	0.01	0.5	MPG435 (O4III(f)) ^e
34 ^c	19.55	-0.04		-0.28			0.11	2.0	<i>B9V</i>
36 ^c	19.29	0.10	-0.46				0.10	1.7	2MASS 0059123-721617
37	18.73:	0.80:		0.23:	0.62:	0.85:	0.15	0.6	
39	20.57:	0.73:		-0.76:	2.36:	1.60:	0.42	2.3	
41	11.32	-0.32	-0.88	0.13	-0.10	0.03	0.01	0.3	HD 5980 (LBV)
45 ^f	21.24:	0.45:		0.07:	0.16:	0.24:	0.64	0.4	
46	19.42	0.55	0.00:	0.46	0.52	0.98	0.07	0.9	

Table 5: (continued)

48	19.54:	0.87:		0.19:	0.72:	0.91:	0.21	1.1	
50	19.42	2.19		0.88	1.67	2.55	0.09	0.9	2MASS 0059431-721307
53 ^f	20.41	-0.11	-0.65:				0.13	1.4	
56 ^f	20.86	0.25:		0.60	0.38:	0.98:	0.05	1.6	<i>A3V</i>
57	18.08	0.05	0.13	0.08			0.01	1.3	
59 ^f	19.26	0.60	-0.29	0.46			0.10	1.1	
60 ^f	21.32:	1.07:		0.83:	1.08:	1.91:	0.23	1.1	
61 ^a	18.87	-0.07		0.42			0.08	1.2	<i>B7-8V</i>
63 ^a	20.82:	0.32:	-3.60:	-0.22:	1.42:	1.20:	0.22	2.0	
64	21.03:						0.39	1.0	
65	19.55	0.88		0.32			0.09	1.3	
68	16.73	-0.11	-0.84	-0.09	-0.22	-0.31	0.01	2.9	<i>B2V</i> , S010202096809, 2MASS 0100370-721315
69 ^g	17.82	-0.13	-0.68	-0.06	-0.06	-0.12	0.02	1.4	<i>B3V</i> , S01020208968
70	15.81	0.00	-0.95	0.08	0.05	0.14	0.02	0.6	[MA93]1240 ^h <i>late O, early B star</i>
71 ^g	18.42	0.05		0.24	-0.02	0.23	0.10	2.3	<i>B6V</i> , S010202010679

^aclosest within a group^b=S010202013449, 2MASS 0057504-720756, USNO-A2.0
0150-00634949^cnorthern component of double^d=S01020202934, 2MASS 0058502-721713^e=2MASS 0059045-721024, cluster's core^ffaint^gbrightest in a group^h=S010202016442, 2MASS 0101029-720658

Table 6: Periods and separations of the optical variable counterparts found in the MACHO database. In the last column, a letter in parentheses indicates in which band the period was found: ‘B’ refers to the blue lightcurve, and ‘R’ to the red one.

Src	MACHO id	Sep.	Period(s)
11 ^a	207.16490.238	1.56"	357 d (R & B)
	207.16490.370	1.68"	357 d (B)
27	207.16546.22	2.57"	9.12 d (R & B)
48 ^b	207.16547.618	1.90"	227 d (R), no data in B
68	206.16661.96	1.35"	long-term variable (B)
70	206.16663.16	1.13"	~1300 d (R & B)

^aSuspiciously close to $P=1$ yr.

^bUnusual lightcurve : the scatter increases towards the maximum.

This figure "f1.jpg" is available in "jpg" format from:

<http://arxiv.org/ps/astro-ph/0212197v1>

This figure "f2.jpg" is available in "jpg" format from:

<http://arxiv.org/ps/astro-ph/0212197v1>

This figure "f6.jpg" is available in "jpg" format from:

<http://arxiv.org/ps/astro-ph/0212197v1>